PROCEEDINGS OF SPIE

SPIEDigitalLibrary.org/conference-proceedings-of-spie

Studies of local shock effects on Shack-Hartmann and digital holography wavefront sensors

Ethan Chu, Timothy Bukowski, Stanislav Gordeyev

Ethan D. Chu, Timothy J. Bukowski, Stanislav Gordeyev, "Studies of local shock effects on Shack-Hartmann and digital holography wavefront sensors," Proc. SPIE 12693, Unconventional Imaging, Sensing, and Adaptive Optics 2023, 1269317 (3 October 2023); doi: 10.1117/12.2677627

SPIE.

Event: SPIE Optical Engineering + Applications, 2023, San Diego, California, United States

Studies of local shock effects on Shack-Hartmann and digital holography wavefront sensors

Ethan D. Chu[a], Timothy J. Bukowski[a], and Stanislav Gordeyev[a]

[a]University of Notre Dame, Notre Dame, IN, United States

ABSTRACT

At supersonic speeds, shock waves create steep gradients in the density of the flow field. These large gradients have been shown to adversely affect the accuracy of Shack-Hartmann Wavefront Sensor (SHWFS) during wavefront reconstruction. This is caused by higher-order beam distortions within the lenslet. In the presented work, the wavefront of a collimated beam propagating through a local shock region over a partially protruding cylinder body was measured using SHWFS and off-axis Digital Holography Wavefront Sensor (DHWFS). These measurements were taken simultaneously allowing for direct comparison. Further study was done on computational and post-processing methods of handling the higher order aberrations caused by the shock, as well as studying their effects on the resulting wavefront. By varying the incoming transonic Mach numbers, the shock strength and spatial extent could be adjusted, thus providing multiple scenarios for comparison. The experimental data presented in this work provides valuable insight into shock-induced effects on the resulting wavefront. These results help to further support the development of new methods for mitigating the adverse effects of shocks on well-established measurement methods such as SHWFS and off-axis DHWFS in similar applications.

Keywords: Shack-Hartmann, Digital Holography, higher-order moment analysis, wavefront reconstruction

1. INTRODUCTION

The Shack-Hartmann Wavefront Sensor (SHWFS) was initially developed by Johannas Franz Hartmann who used an opaque screen with an array of holes. This was further developed by Roland Shack and Ben Platt in 1971[1] who exchanged the screen with an array of micro lenses. The development of the SHWFS was motivated by the need to accurately measure and correct optical aberrations in telescopes, particularly in astronomical observations. The SHWFS has found widespread use in adaptive optics systems, which are employed to correct for atmospheric turbulence and other aberrations in real-time. By continuously monitoring the wavefront distortions and feeding the information to deformable mirrors or lenses, adaptive optics systems can dynamically correct for these aberrations, resulting in sharper images and improved resolution in various optical applications.

Over the years, the SHWFS has also been utilized in other fields. In ophthalmology, it is used to evaluate the optical aberrations in the human eye and aid in the customization of corrective lenses. It also helps with assessing the quality of laser beams by measuring their wavefront distortions for laser beam characterization. There has been a considerable amount of research into the integration of laser propagation systems into airborne platforms.[2–5] A large interest is in higher speed transonic and supersonic flow regimes, where shocks can form a sharp change in density, thereby affecting the index of refraction and having a significant effect on beam propagation. Kalensky et al.[6,7] have shown that the presence of the shock will deteriorate the performance of SHWFS. As a reminder, SHWFS is comprised of an array of subaperture lenslets focused onto a camera sensor. The average gradient of the incoming phase aberration over each subaperture in the pupil plane is estimated from displacements of diffraction-limited irradiance-pattern, simply referred to as dots, in the image plane.[6] These slope estimates are traditionally used in a least-squares reconstructor to estimate the continuous wavefront aberration.[8] Recently, Kalensky et al.[7] analytically showed how the density discontinuity of a shock crossing a subaperture lenslet leads to a distorted far-field irradiance pattern, resulting in "smeared" or bifurcated dots. This effect has also been shown to occur in experiments.[9,10] It was then shown through wave-optics simulation how these distorted dots affect wavefront reconstruction.[7] In Reference 11, Kalensky used second-moment to quantify the spatial spreads of the dots in a Shack-Hartmann irradiance pattern, which allowed him to find dots distorted by higher order aberration, and, in the case of that work, branch-points. In the work presented here, this approach is expanded to even higher order spatial statistics to study their ability to find the affected lenslets,

Unconventional Imaging, Sensing, and Adaptive Optics 2023, edited by Jean J. Dolne, Mark F. Spencer, Santasri R. Bose-Pillai, Proc. of SPIE Vol. 12693, 1269317
 · 0277-786X · doi: 10.1117/12.2677627

and possibly provide additional information to aid in wavefront reconstruction. Higher order spatial statistics of the irradiance-patterns have been used before in literature to improve wavefront reconstruction, where they were related to affine coefficients which were then used to reconstruct the wavefront.[12]

In this paper we discuss the issues of SHWFS that arise in situations where underlying measured wavefronts are not smooth, specifically when created from local shock waves in transonic flows, and different approaches to work around these conditions. In Section 2 we discuss the theory and equations used for Shack-Hartmann and digital holography. In Section 3 we describe the experimental setup we used to create the local shock and to take simultaneous Shack-Hartmann and digital holography wavefront measurements. Section 4 discusses the statistics of the Shack-Hartmann dot pattern which were used to mask out the shock and compare the wavefronts from the two sensors. Finally, our findings are summarized in Section 5.

2. SENSOR WAVEFRONT RECONSTRUCTION

2.1 Shack-Hartmann Wavefront Sensor

2.1.1 SHWFS Wavefront Reconstruction

As discussed previously, the SHWFS uses a lenslet array to create an array of dots on a sensor to measure a wavefront. For an unaberrated planar wavefront, the diffraction-limited irradiance pattern will contain a grid of regularly spaced dots. When the wavefront is disturbed, the individual dots will be displaced from the optical axis of each lenslet, as shown in Fig. 1. Using this displacement, we can calculate the local wavefront slope as

$$\left(\frac{\partial w}{\partial x}\right)_k \approx -\frac{\Delta x}{f_k}, \left(\frac{\partial w}{\partial y}\right)_k \approx -\frac{\Delta y}{f_k}, \tag{1}$$

where $\left(\frac{\partial w}{\partial x}, \frac{\partial w}{\partial y}\right)$ is the two-dimensional wavefront slope over a subaperture lenslet, k is the lenslet number, and f_k is the lenslet focal length. The wavefront is reconstructed by solving a discretized version of Eq. 1 using the Southwell reconstructor algorithm.[13] Lastly, instantaneous global tip, tilt, and piston components are removed from the wavefront.

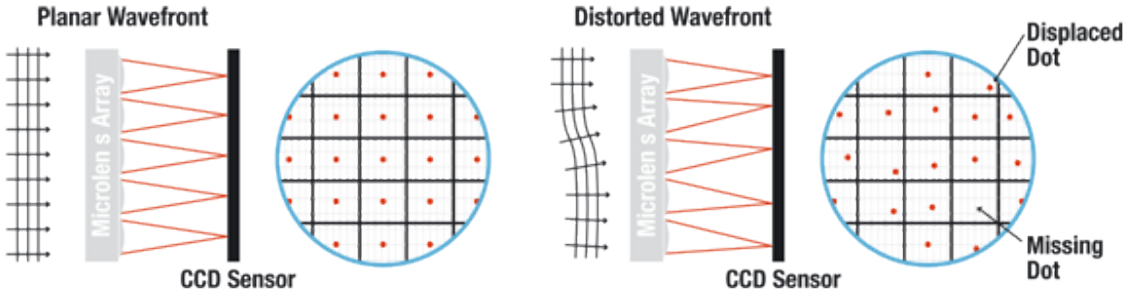

Figure 1: A principle of operation of Shack-Hartmann WFS. For a planer wavefront (left plot), the dots on the image plane are regularly spaced. When a distorted wavefront is passed through the lenslet array (right plot), the dots are displaced. Source: ThorLabs.com[14]

2.1.2 Procedure for calculating higher-order moments

A key assumption in the wavefront reconstruction process is that tilt is calculated from the shift in the dot position, referred to as a centroid tilt or C-tilt,[15] is equal to the average tilt in the wavefront at the lenslet pupil plane, G-tilt.[16] However, when there is a discontinuity across the lenslet, the irradiance pattern bifurcates or smears, and C-tilt is no longer a good estimate of G-tilt.[7] Since the wavefront is constructed through a least-squares reconstructor, these contaminated tilt measurements affect the accuracy of the entire reconstructed wavefront.

In Ref. 11, the spread in irradiance patterns caused by higher order aberration across the lenslet was quantified using the second central moment. Through this we can identify which points have been corrupted by the shock-related distortions and exclude them from the reconstruction, thereby increasing accuracy. The ultimate goal would then be to go back and use additional information to reconstruct the wavefront for the excluded points. In this paper, we extend this idea to also look at the third and fourth central moments to study how to best identify contaminated lenslet irradiance patterns.

The traditional Shack-Hartmann wavefront analysis breaks the irradiance pattern into areas of interest (AOI) behind each lenslet. The centroid of the dot within each AOI can then be calculated to find the dot displacment. The centroid is calculated as[17]

$$\overline{x} = \frac{\int_{-\infty}^{\infty}\int_{-\infty}^{\infty} I(x,y)\, x\, dxdy}{\int_{-\infty}^{\infty}\int_{-\infty}^{\infty} I(x,y) dxdy}, \quad \text{and} \quad \overline{y} = \frac{\int_{-\infty}^{\infty}\int_{-\infty}^{\infty} I(x,y)\, y\, dxdy}{\int_{-\infty}^{\infty}\int_{-\infty}^{\infty} I(x,y) dxdy}, \tag{2}$$

where $I(x,y)$ is the intensity of each pixel, x and y are the location of the pixel within the AOI, and $\overline{x}$ and $\overline{y}$ are the relative locations of the centroid. This is also referred to as the first moment of the distribution within the AOI. The second central moment, sometimes called the variance, is more commonly used in the form of standard deviation and is found by

$$\mu_{2,x} = \frac{\int_{-\infty}^{\infty}\int_{-\infty}^{\infty} I(x,y)\,(x-\overline{x})^2\, dxdy}{\int_{-\infty}^{\infty}\int_{-\infty}^{\infty} I(x,y) dxdy} \quad \text{and} \quad \sigma_x = \sqrt{\mu_{2,x}} \tag{3}$$

where $\mu_{2,x}$ is the second central moment in x and σ_x is the standard deviation in x. The same process is applied to the y direction. This quantity represents the relative width of the intensity distribution in the x and y direction.

The third central moment gives us the skewness of the distribution within the AOI. Skewness describes an asymmetry of the irradiance pattern. This is defined by the following

$$\mu_{3,x} = \frac{\int_{-\infty}^{\infty}\int_{-\infty}^{\infty} I(x,y)\,(x-\overline{x})^3\, dxdy}{\int_{-\infty}^{\infty}\int_{-\infty}^{\infty} I(x,y) dxdy} \quad \text{and} \quad Skew_x = \frac{\mu_{3,x}}{\sigma_x^3} \tag{4}$$

where $\mu_{3,x}$ is the third central moment in x and $Skew_x$ is the skewness in x. Skewness shows asymmetry in the intensity distribution pattern.

The fourth central moment is used to identify the "tailedness" of the distribution; that is a measure that relates to the tails of a distribution. Higher kurtosis values indicate a greater presence of extreme deviations (or outliers) in the data. In the presence of a sharp gradient, the dots are usually distorted in some extreme fashion which increases the presence of these outliers. Kurtosis allows us to quantify the "spread" of the distribution for these distorted dots. This is defined as

$$\mu_{4,x} = \frac{\int_{-\infty}^{\infty}\int_{-\infty}^{\infty} I(x,y)\,(x-\overline{x})^4\, dxdy}{\int_{-\infty}^{\infty}\int_{-\infty}^{\infty} I(x,y) dxdy} \tag{5}$$

$$Kurt_x = \frac{\mu_{4,x}}{\sigma_x^4} \tag{6}$$

where $\mu_{4,x}$ is the fourth central moment and $Kurt_x$ is the kurtosis in x. In further discussions, μ_4 refers to the fourth central moment and $Kurt$ as the relative kurtosis as it has been normalized by σ.

2.2 Digital Holography Wavefront Sensor

While the SHWFS measures the wavefront slopes, Digital Holography Wavefront Sensors (DHWFS) allow us to directly measure the complex optical field of the beam. Our setup uses an off-axis image plane geometry setup where the signal beam is interfered with a tilted reference beam onto a camera sensor creating a fringe patterned intensity field. An example image is shown in Fig. 2a with a zoomed in window showing the fringe pattern. This process is described in further detail in Wilcox at al.[18]

The total intensity of the fringe pattern, I, is the superposition of the complex optical fields for signal and reference beams, U_S and U_R, respectively. This is defined as

$$I = |U_S + U_R|^2 = |U_S|^2 + |U_R|^2 + U_S U_R^* + U_S^* U_R.$$

$|U_S|^2$ and $|U_R|^2$ are the zeroeth-order terms which are ignored as they do not contribute to the phase information. $U_S U_R^*$ and $U_S^* U_R$ contain the phase information we desire. The $(*)$ denotes complex conjugates, thus $U_S U_R^*$ and $U_S^* U_R$ are simply complex conjugates of each other and we only need one pair to find the optical complex field. To isolate one term, $U_S U_R^*$, we perform a Fourier transform on the fringe pattern (Fig. 2a). This gives us Fig. 2b. We can then filter out all the other unwanted terms (i.e. $U_S^* U_R$, $|U_S|^2$ and $|U_R|^2$) by selecting only the off-axis peak circled in red in Fig. 2b.

Mathematically, this process is shown as

$$U_S(x, y) = A_S \exp[i\phi_S(x, y)]$$

and

$$U_R^*(x, y) = A_R \exp[-i\phi_R(x, y)] \exp\left[-i\frac{2\pi}{\lambda z}(x_R x + y_R y)\right] \tag{7}$$

where A_S and A_R are the amplitude of the signal and reference beam, respectively, x and y is the coordinate system co-planer with the propagating wavefront at the source of the beam, ϕ_S and ϕ_R is the phase of the signal and reference beams, λ is the laser wavelength, z is the propagation distance (i.e. the distance from the object to the sensor), and x_R and y_R is the coordinate system at the focal plane of the reference beam. The extra terms in Eq. 7 describes the tip/tilt in the reference beam.

After isolating $U_S U_R^*$, we remove tip/tilt component, introduced by the reference beam, by shifting it to the middle of the Fourier plane, then perform the inverse Fourier transform.

$$\mathscr{F}^{-1}\{U_S U_R^*\} = \mathscr{F}^{-1}\left\{A_S A_R \exp[i(\phi_S - \phi_R)] \exp\left[i\frac{2\pi}{\lambda z}(x_R x + y_R y)\right]\right\}$$

This is done first for a "no flow" case with the tunnel off to get the complex optical field of the optics system, which we can then remove from the flow on cases. The resulting amplitude and phase fields are shown in Fig. 3a and 3b. However, at this point the phase is wrapped between $-\pi$ and π and must be unwrapped before it can be related to OPD by

$$OPD = \phi\frac{\lambda}{2\pi}$$

As with the SHWFS, the instantaneous global tip, tilt, and piston components are then removed from the wavefront.

In unwrapping the phase, there were two methods that we considered. The first method was developed by Herráez et. al.[19] and prioritizes unwrapping based on pixel reliability. This method works well for relatively smooth phase patterns such as the no-flow case. However, with more complicated phase patterns or increased noise, this method will incorrectly unwrap in some spots, leaving behind patchy discontinuities which can be

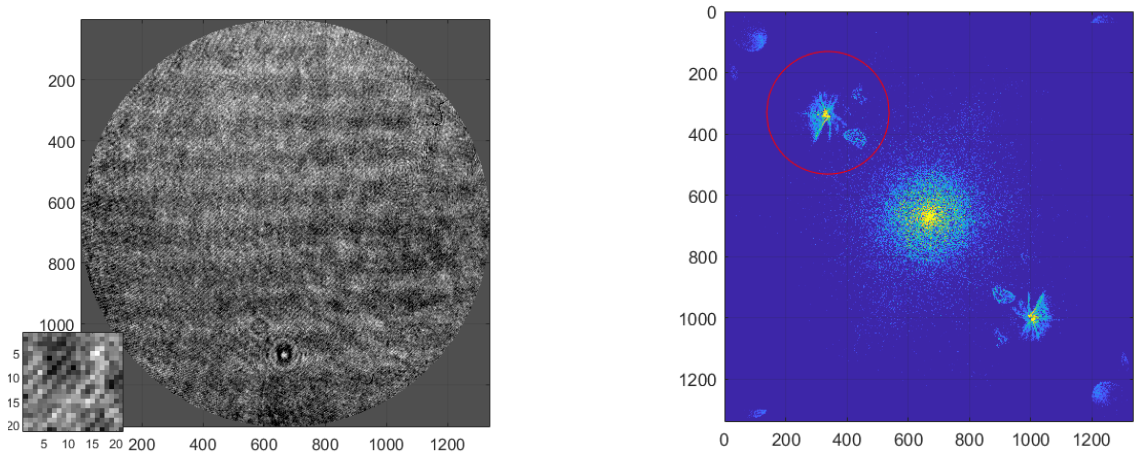

(a) (b)

Figure 2: (a) Example recorded hologram with zoomed in window showing fringes. (b) 2-dimensional Fourier transform of the hologram. Only the region circled in red is kept for analysis.

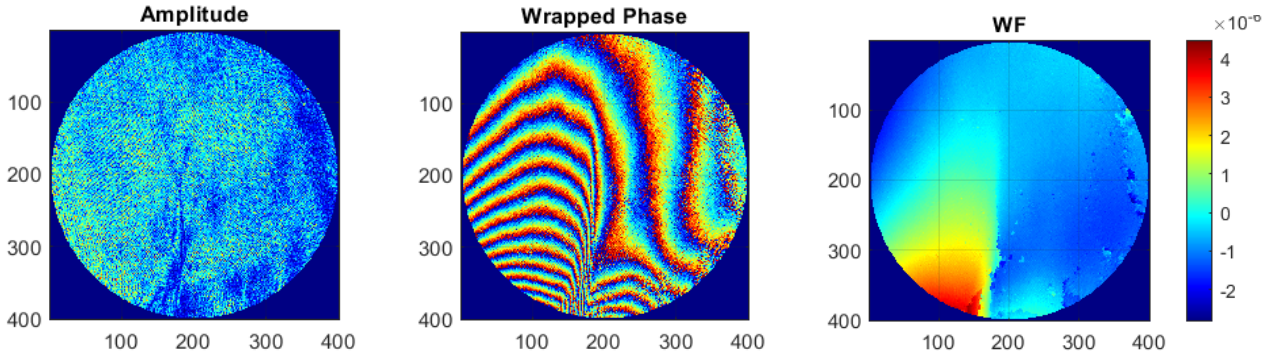

(a) (b) (c)

Figure 3: (a) Amplitude map of the fringe pattern. (b) The wrapped phase of the signal beam. (c) The unwrapped phase or reconstructed wavefront.

seen in Fig. 3c. Filtering the complex optical field was attempted to try to decrease noise and to better unwrap the phase, but it only had a marginal effect. The second method is a least squares-based unwrapper. By nature this method always creates a continuous phase; however, it introduces greater error in the wavefront, especially in regions with steep gradient. We chose the Herráez method, as the error resulting from points missed during unwrapping are much more obvious and easy to disregard.

3. EXPERIMENTAL SETUP

The wind tunnel used in the experiments is located at the Hessert Laboratory for Aerospace Research at the University of Notre Dame. The tunnel is driven by up to two vacuum pumps with variable speeds. The test area had a 4x4 inch cross-section. In order to create a shock, a partial cylinder with a 100-mm diameter curvature and 25 mm high, was installed in the test section, see Fig. 4a. The cylinder insert locally accelerates the flow to supersonic speeds to produce a localized shock right at the peak of the cylinder. The size and strength of this shock, and thus the degree of the resulting wavefront local gradient in the shock area, can be adjusted by increasing or decreasing the flow speed. For our system, the freestream velocity was measured to be Mach 0.45 at the point where the local shock appeared above the partial cylinder. For more information on this flow field is provided in Ref. 20.

The schematic of the experimental setup is presented in Fig. 5. The laser emitter used was a Torus 532nm green laser. The collimation tube expands the pencil beam of 1.7 mm ($\approx 1/16$ in) into a 25.4mm (1 in) beam.

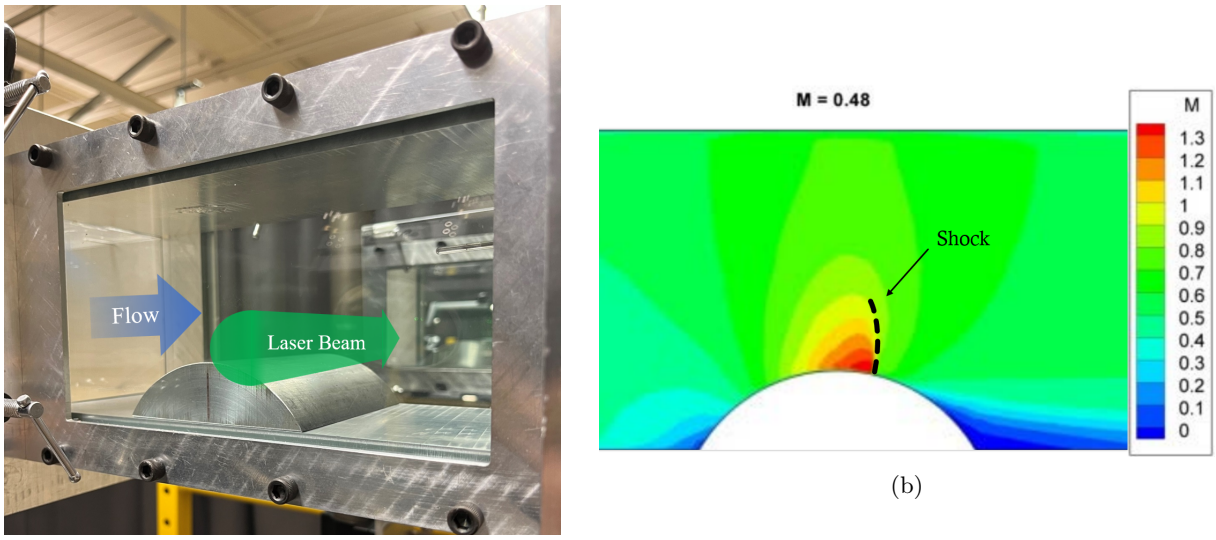

(a) (b)

Figure 4: (a) Tunnel test section with 2-D partial cylinder. (b) CFD simulation[20] showing transonic flow over partial cylinder with shock marked by dashed line.

BC1 splits the beam into the reference beam for the DHWFS and the signal beam. Passing the signal beam through L1 and L2 expands the beam to 51mm (2 in). The expanded beam passes through the wind tunnel and returns back through the tunnel to L1 and L2, reducing the beam. This becomes the signal beam and is returned through BC1 and reflected to L3 and L4, which are used for re-imaging. The iris is used to eliminate as much of the ghost images from the acrylic windows as much as possible. The reference beam is expanded through L5 and L6 to fully cover the DHWFS camera sensor, allowing for maximum signal recovery. BC2 is used to split the signal beam to both the SHWFS and the DHWFS cameras. BC3 combines the signal and reference beams, and has an adjustable platform which allows tip/tilt to be added to the reference beam. The resulting fringe pattern is captured on a Phantom v1840 high speed, high resolution camera with a resolution of 1952 x 2048 pixels and a pixel size of 13.5 μm.

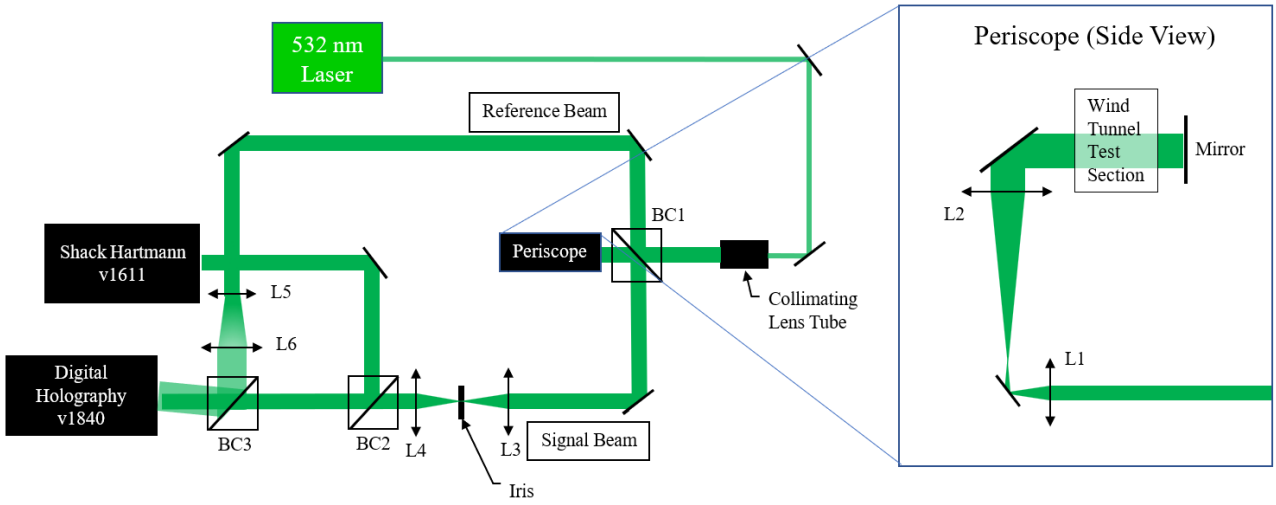

Figure 5: Experimental setup for capturing shock.

The Shack-Hartmann dot patterns were captured using a Phantom v1611 high-speed camera with the reso-

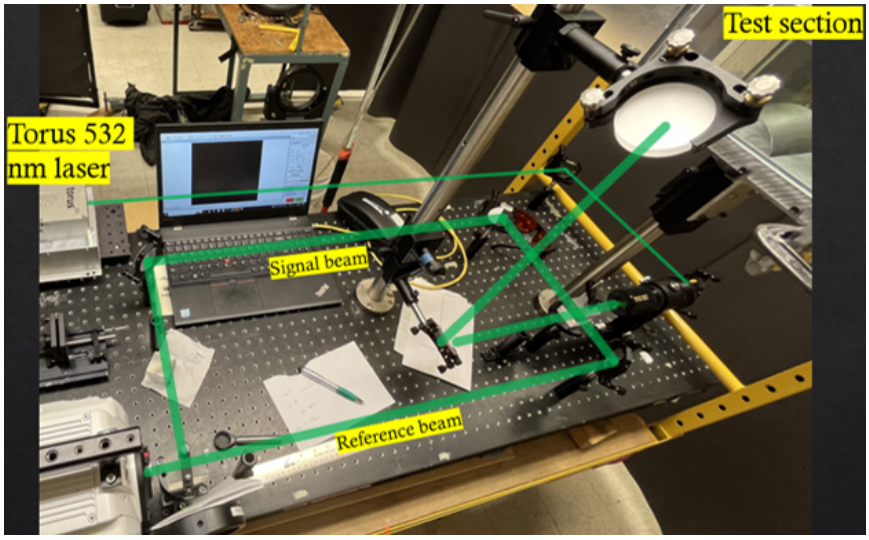

Figure 6: Tunnel setup showing test section and optical components. This only shows the setup for the digital holography. Shack-Hartmann WFS was added on later.

lution of 768 x 768 pixels with a pixel size of 28 μm. The camera was equipped with a microlenslet array. The individual lenslets were square in shape and measured at 0.3x0.3 mm with a focal length of 38.2 mm. This will provide an image that is divided into an array of sub-apertures or AOIs, each approximately 11x11 pixels.

This setup allowed us to simultaneously capture an instantaneous wavefront using both Shack-Hartmann and digital holography. As shock-related discontinuities will affect the reconstructed wavefront differently for these sensors, by comparing the wavefronts we can address the effects of the local discontinuities on the wavefront reconstruction algorithms.

The cylinder geometry was chosen, as this flow field only has a small region that is accelerated to be supersonic, and the resulting shock is only a few inches long. CFD simulation for this flow field is shown if Fig. 4b, where the color represents Mach number. This small shock is beneficial for both sensors as it allows a continuous path between the upstream and downstream sides of the shock. For the SHWFS this means we can crop out the dots contaminated by the shock effects, and then reconstruct the wavefront only using the other dots, which will give a wavefront that is much more accurate. With the DHWFS, there is a path of gradual increase in phase around the top of the shock, which allows us to unwrap the phase, even if there is a very sharp phase gradient at the base of the shock. Additionally, the shock decreases in strength further from the cylinder, which allows us to see a variety of shock strengths in a single measurement.

4. RESULTS

4.1 SHWFS - DHWFS Comparison

First, we chose a matching frame from the SHWFS and the DHWFS that captured a reasonably clean shock wave. The SHWFS dot pattern of this frame is captured in Fig. 7. However, to compare the reconstructed wavefronts from the two sensors, we had to do additional preprocessing. The resolution of the DH wavefront was reduced to match the Shack-Hartmann wavefront through interpolation using the *imresize* MATLAB function. The reconstructed wavefronts of the SHWFS and DHWFS were then aligned by eye; in the future experiments we will use a physical marker that we will place in a conjugate plane which we can then use to align the wavefronts. The alignment, global tip, tilt, and piston components were then removed from the wavefronts. Representative wavefronts, simultaneously measured by SHWFS and DHWFS, are shown in Fig. 8a and 8b, respectively.

Visually, there is a clear difference between these two wavefronts. The SH wavefront does see a steep increase in the wavefront, however, the ramp is attenuated and the overall change in wavefront is much less for the SH wavefront than the DH wavefront. This is more clearly shown in Fig. 8d where cross-sections of the two

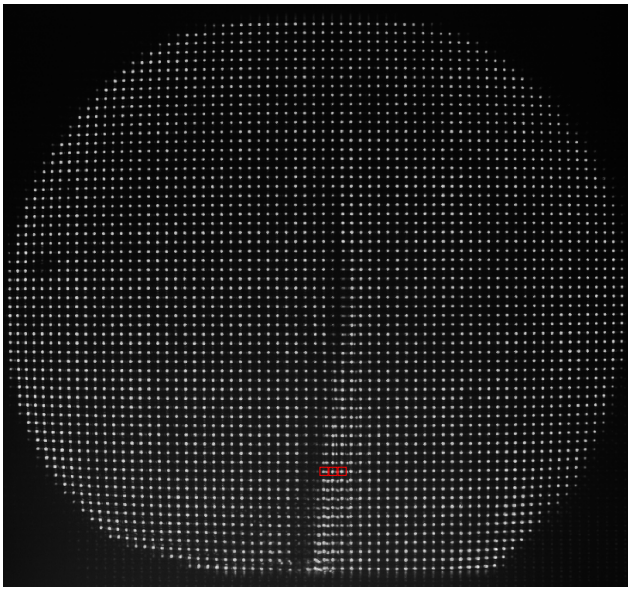

Figure 7: Shack-Hartmann dot pattern with flow on. The shock region in the middle of the image is clearly visible. The red boxes show selected distorted points, later re-plotted in Fig. 12, to do further analysis on.

wavefronts along the same line are plotted against each other. Since some dots in the Shack-Hartmann image bifurcate, the measured C-tilt is much smaller than the large G-tilt that exists at that point of the wavefront. This leads to a much flatter reconstructed wavefront. The OPDrms defined as the temporal mean of the spatial rms of the DH wavefront was 0.61 μm while only 0.28 μm for the SH wavefront.

As mentioned, a large benefit of using the localized supersonic shock is that if we exclude the bifurcated dots from the SHWFS image, then we can get a more accurate wavefront, since the dots outside the shock region are undistorted and still satisfy the assumptions detailed in Sec. 2.1.1. A very liberal mask excluding points well beyond the shock region was manually applied to the SHWFS image and the wavefront was reconstructed from the masked dot image to demonstrate this. The resulting SH wavefront is shown in Fig. 8c, with the difference between the SH and DH wavefronts shown in Fig. 8e. Here we can see the wavefronts match much better as the masked SH wavefront is able to more accurately follow the measured slope. We can see in Fig. 8d that the two measured wavefronts align much better. The OPDrms in this was also much closer at 0.53 μm for the masked SH wavefront and 0.56 μm for the DH wavefront.

4.2 Shack-Hartmann Statistical Analysis

The next step was to develop an algorithm to detect and mask out the distorted dots from the wavefront without having to manually apply the mask. The "bad" dots are defined as not being distinct diffraction-limited single dots, such as bifurcated dots or smeared dots. Standard Deviation for x- and y-components, as defined in Eq. 3, are plotted in Fig. 9a and 9c, respectively. In Figures 9b and 9d, the standard deviation is normalized by the value from the no flow case, defined as

$$\sigma_{Norm} = \frac{\sigma_F - \sigma_{NF}}{\sigma_{NF}} \tag{8}$$

where σ_{Norm} is the normalized standard deviation, σ_F is the standard deviation of the flow-with-shock condition, and σ_{NF} is the standard deviation of the no-flow condition. The results are shown in Figures 9b

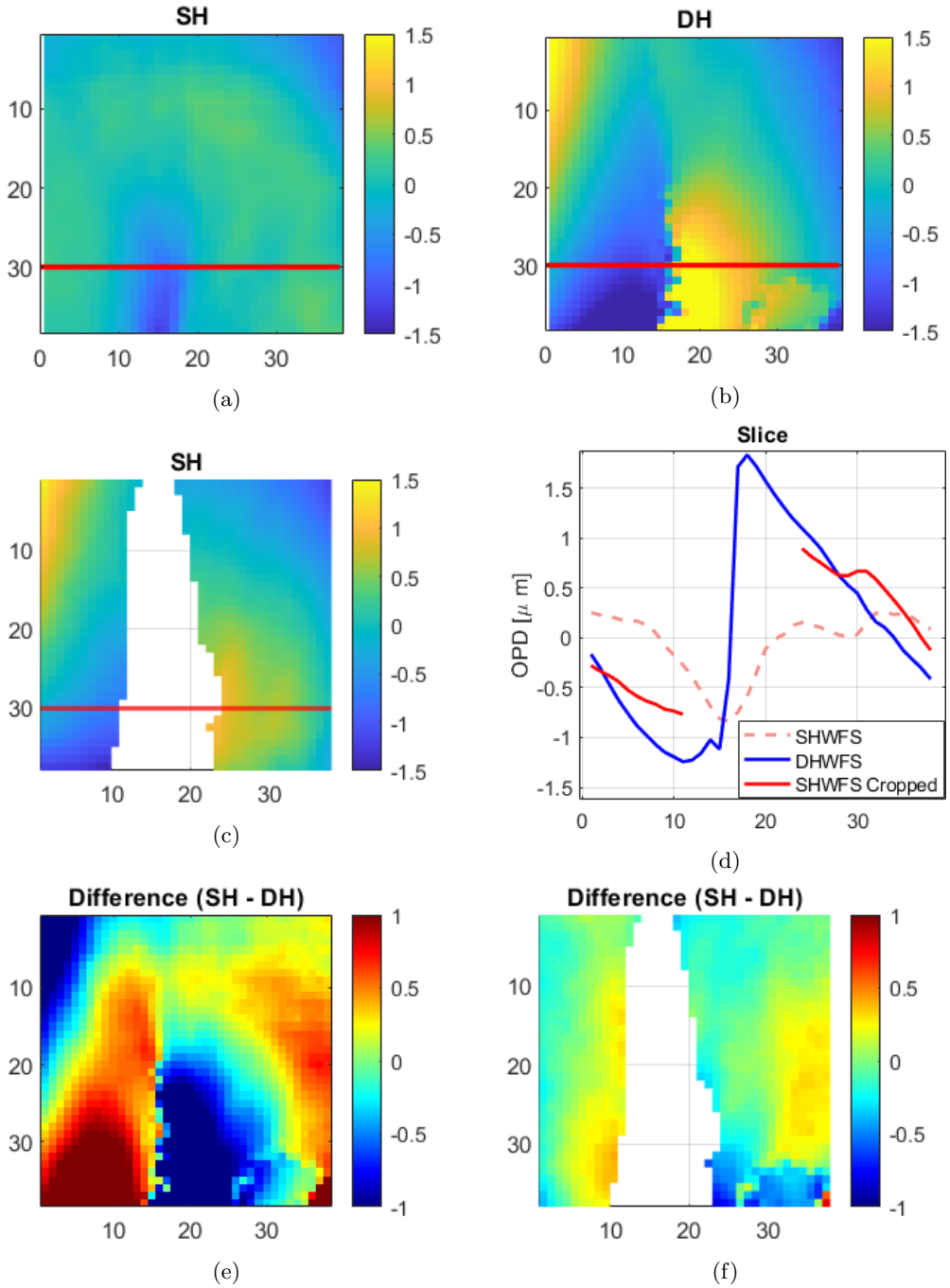

Figure 8: The reconstructed wavefront for (a) the SHWFS and (b) DHWFS. (c) shows the reconstruction for the SHWFS with the mask applied. (d) The cross-sectional slice of Figures 8a, 8b, and 8c, at the red lines drawn on the figures. (e) The percentage difference between the original reconstructed wavefronts of the SHWFS and DHWFS. (f) The difference between the SHWFS and DHWFS after applying the mask over the shock. Colormaps in all plots show the wavefront in microns.

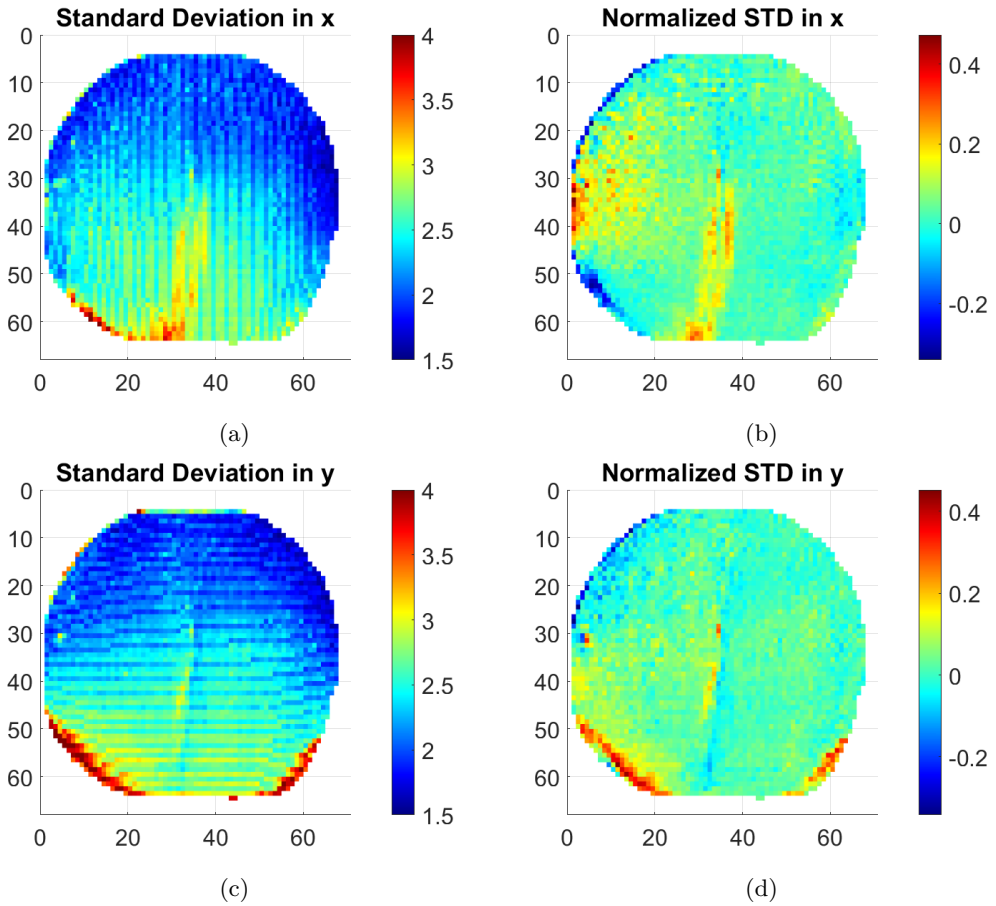

Figure 9: Standard Deviation of the dot pattern as shown in Fig. 7 are shown in their (a) x- and (c) y-components. Standard deviation normalized by no-flow in their (b) x- and (d) y-components.

and 9d. Standard deviation has been successfully used in detecting certain dot distortions as demonstrated by Kalensky's work.[11] For the presented data, though, it was found not to be a reliable method of detecting the distorted dots, as the shock region in Fig. 9 is not well-defined.

Skewness maps in $x0$ and y-directions, defined in Eq. 4, are plotted in Fig. 10a and 10c. The changes in skewness values within the shock region are low, also making it a poor choice of parameter for thresholding in this work. However, it was shown in Ref. 7 that shocks of different strengths will create bidurcated dots with varying peak intensities, which would result in a skewed distribution across the AOI. So, it is possible that the skewness could still be used to gain information regarding the orientation of the shock and its strength. We also applied the normalized skewness, defined in a similar fashion as the normalized standard deviation values in Eq. 8, with the results shown in Fig. 10b and 10d. It was also found not to be a reliable way to identify distorted dots, as the shock region in these plots is barely visible.

As neither the standard deviation nor skewness value were found to be a robust way to identify the distorted dots, we were interested at looking at kurtosis which would potentially be more helpful to identify the "bad" dots. We considered three ways of analyzing the kurtosis quantity: $\mu_{4,x}$ in the x-direction, as defined in Eq. 5, $Kurt_x$ in the x-direction, as defined by Eq. 6, and a normalized kurtosis in the x-direction, $Kurt_{Norm,x}$, defined as,

$$Kurt_{Norm,x} = \frac{Kurt_{F,x} - \sigma_{NF,x}}{\sigma_{NF,x}} \tag{9}$$

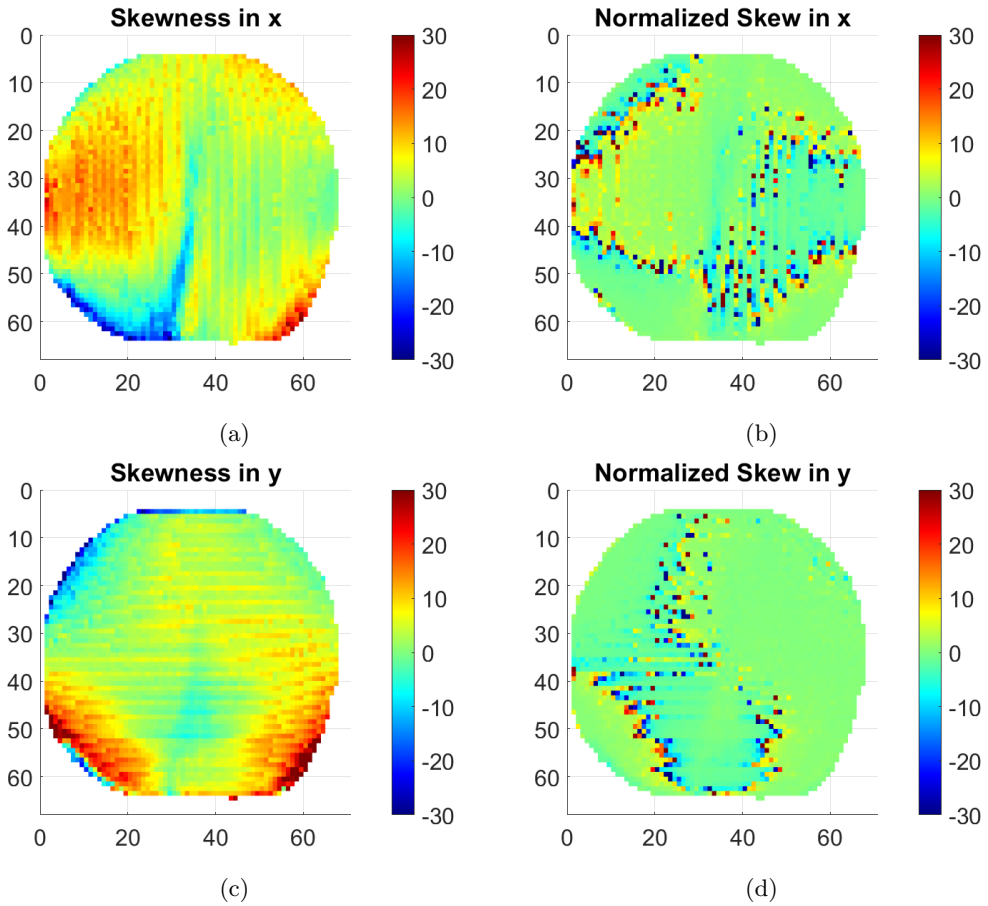

Figure 10: Skewness of the dot pattern as shown in Fig. 7 are shown in their (a) x- and (b) y-components. Skewness normalized by no-flow in their (b) x- and (d) y-components.

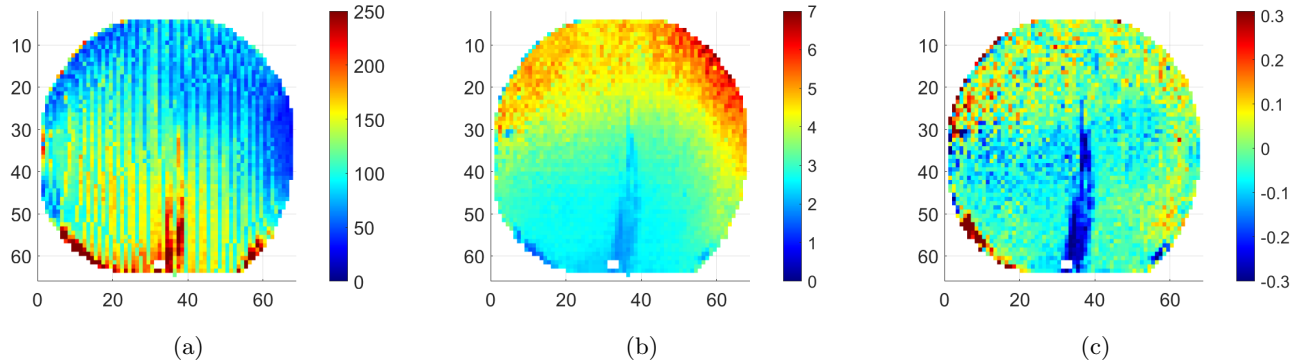

Figure 11: (a) μ_4 in x-direction, as defined in Eq. 5 (b) Kurtosis in x-direction, as defined in Eq. 6 (c) Kurtosis in x-direction normalized by no-flow kurtosis, as defined in Eq. 9.

where $Kurt_{Norm,x}$ is the normalized value of kurtosis, $Kurt_{F,x}$ is the kurtosis of the flow-with-shock condition, and $Kurt_{NF,x}$ is the kurtosis of the no-flow condition. Figures 11a, 11b, and 11c show the kurtosis maps for $\mu_{4,x}$, $Kurt_x$, and $Kurt_{Norm,x}$, respectively. While $\mu_{4,x}$ and $Kurt_x$ do show the shock region relatively clearly, they struggle with capturing the fringes of the shock, particularly the tip of the shock. The normalized kurtosis, on another hand, distinctly showed the shock region with large negative values.

Figure 12 also provides the values for $\mu_{4,x}$, $Kurt_x$ and $Kurt_{Norm,x}$ for the selected dots, identified in Fig. 7,

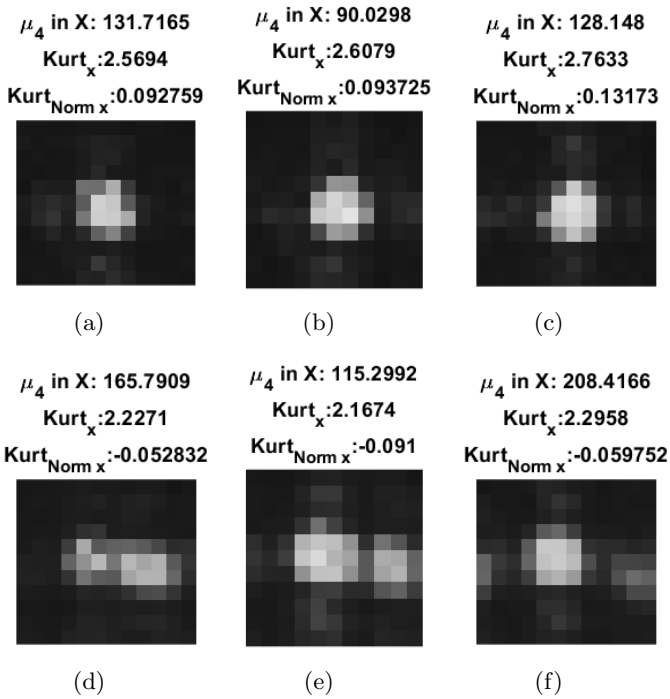

Figure 12: (a), (b), (c) Dots in a no-flow case are relatively uniform. (d), (e), (f) Dots taken inside the shock region show large distortions especially when compared with the no-flow dots. Corresponding values for $\mu_{4,x}, Kurt_x$ and $Kurt_{Norm,x}$ are also given.

for both no-flow and the shock cases. These selected points are of particular interest as they show the distortion caused by the shock. Figures 12a, 12b, and 12c shows the dots in the no-flow case where the dots are relatively uniform. Figures 12d, 12e, and 12f show the same dot for the shock case; the dots are clearly distorted and even bifurcated. The kurtosis-related values of the dots is larger than for the diffraction-limited dots. Thus, we can conclude that these dots have a more flat-topped distribution around the centroid. This is due to the dot smearing and dot splitting as a result of shock. The distortion on the dots can also cause dots to partially deflected into their neighboring AOIs.

We manually adjusted through a range of thresholds to see at what value the shock region is eliminated. The selected thresholds were somewhat subjective as we visually inspected whether "bad" dots were eliminated. After applying the thresholds, we can create a mask of the points we want to keep or eliminate. This mask is what we use for wavefront reconstruction.

Figure 13a is the mask based on $\mu_{4,x}$ after the threshold is applied. This mask was found to be the most conservative in removing distorted dots. There were still many distorted dots that were undetected. The black box indicates the region that was extracted and rescaled for comparison with the DH wavefronts as described in Sec. 4.1. The red dotted line is where the cross-sectional slice of both SH and DH wavefronts were taken for comparison. From the cross-sectional slice of the reconstructed wavefront in Fig. 13d, the improvement was so small that it is almost negligible.

Figure 13b shows the mask using $Kurt_x$. This mask removes more points from the shock region than the mask using $\mu_{4,x}$, which slightly improved the wavefront accuracy, as indicated in Fig. 13e. For both of these cases, when trying larger values of the thresholds, it began eliminating more points outside of the shock region. Thus, increase the thresholds did not improve the final reconstruction of the wavefront.

The most promising mask is based on the normalized kurtosis, Eq. 9, shown in Fig. 13c. Visually, the mask based on $Kurt_{Norm,x}$ was able to identify more of the shock region than the $\mu_{4,x}$- and $Kurt_x$-based masks. The reconstructed wavefront, presented in Fig. 13f, also shows a better agreement with the DH wavefront.

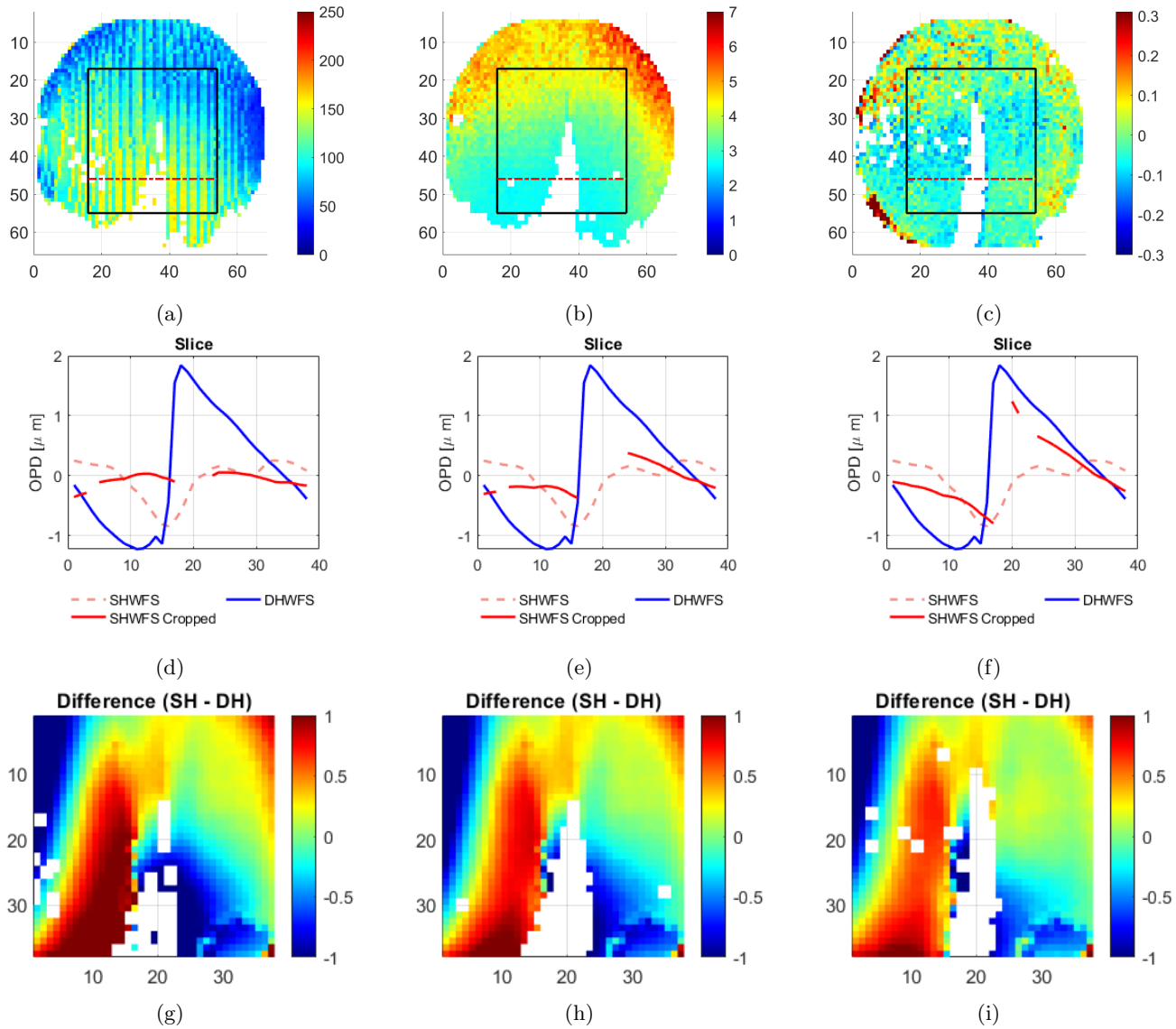

(a) (b) (c)

(d) (e) (f)

(g) (h) (i)

Figure 13: (a),(b),(c) The colormap masks based on $\mu_{4,x}$,$Kurt_x$, and $Kurt_{Norm,x}$, respectively, after applying the thresholds. (d),(e),(f) Cross-sectional slices of the SH and DH reconstructed wavefronts, comparing the SHWFS and DHWFS reconstruction using masks based on $\mu_{4,x}$, $Kurt_x$, and $Kurt_{Norm,x}$, respectively. (g),(h),(i) The percent difference between the SH and DH reconstructed wavefronts.

However, there are still some points on the fringes of the shock that were not identified. We hope to better refine this process and perhaps use some combination of these different kurtosis methods to fully capture the shock-distorted dots. More information may also be gleaned from the second and third central moments and perhaps a combination of all of these would provide a better and cleaner mask to eliminate distorted dots.

Figures 13g, 13h, and 13i, shows the difference between the SH and DH reconstructed wavefronts. The dark red and blue indicated large deviations from the DH wavefront. Ideally, the error would be zero as indicated by the green, with the mask based on $Kurt_{Norm,x}$ showing the greatest improvement out of all three applied masks. The accuracy of the identifying the shock region maybe improved upon if some combination of the three kurtosis values or additions of lower moments.

We also attempted to create a single moment map by applying the root-sum-square method to find the

absolute value of the x- and y-components. However, since the y-component did not contribute much in terms of identifying the shock region, neither the absolute values of standard deviation, skewness, nor kurtosis consistently improved our results. While we are not completely dismissing the y-component, we decided to focus more on the x-component of the moments for the purposes of proving this concept.

As a final note, while the partial cylinder has many benefits making it an attractive geometry to use in experiments, it may not be the best option. When the signal beam passes through the shock over the cylinder, aero-optical distortions are integrated along the spanwise extent of the shock which spans the entire width of the tunnel test section. This causes a very large jump, on the order of over 10π, in aero-optical phase across the shock region, which causes significant refraction effects on the dot pattern. This was visible in some SHWFS images where there was a significant loss of intensity near the shock, as observed in Fig. 7. Further analysis is required to study how this propagation through a discontinuous volume affects the SHWFS irradiance pattern compared to the simulation done in Ref. 7, which has a discontinuity only on a conjugate plane without having to propagate through additional regions of different indexes of refraction. Additionally, due to the incoming turbulent boundary layer over the cylinder, the shock was not perfectly spanwise-uniform, which resulted in the shock not being perfectly straight in the spanwise direction. Thus thick or duplicate shocks may appear, increasing the number of distorted points and creating an environment that is more difficult for elementary shock-tolerant re-constructors to handle. However, by using a hemisphere in future experiments, we can reduce the spanwise width of the shock, potentially alleviating the severity of phase jumps and simplifying the shock geometry.

5. CONCLUSION

Wavefront sensors such as Shack-Hartmann wavefront sensor (SHWFS) and digital holography wavefront sensor (DHWFS) have been very useful in measuring aero-optical disturbances. However, large density gradients in the flow field can adversely affect the Shack-Hartmann wavefront sensor's ability to accurately reconstruct the optical wavefront. We performed a series of experiments in transonic flow, where a local supersonic region with an ending shock was formed over a two-dimensional partial cylinder. When a collimated laser beam was propagated in the spanwise direction through the shock wave, it resulted in a large gradient in the wavefront across the shock region. This gradient created significantly distorted dots in the shock region, making the SHWFS reconstruction algorithm return a false wavefront. Using the images from the experiments, we attempted to correctly reconstruct the wavefront despite the large gradient. A digital holography sensor was also used to simultaneously measure the same wavefronts in conjunction with the SHWFS.

In the results discussed above, we manually eliminated the distorted dots by visual inspection as well as using statistical values to identify the shock. Our goal was to develop a method that was able to identify distorted dots, related to the large spatial gradients caused by supersonic shocks, using higher-order statistics of dot images. While skewness was not very effective at highlighting the shock, it may be useful for finding the strength and orientation of the shock. Kurtosis and standard deviation both performed decently well in identifying the shock. Normalizing kurtosis by the no-flow case also showed great potential in this regard as well. Thus, we demonstrated that using a kurtosis-based mask allows us to identify and eliminate distorted dots affected by the shock wave.

After eliminating these points by applying different masks, we compared the reconstructed wavefronts to the wavefront measured by digital holography to see if the accuracy of the Shack-Hartmann wavefront reconstruction is improved. With the digital holography technique, reconstruction around the shock is not affected by the shock itself, thus the DHWFS is allows us to compare the accuracy of reconstructed SH wavefronts before and after masking out the shock. We've shown that after eliminating the main region of the shock, we can obtain agreeable wavefronts between the SHWFS and DHWFS. We can thus conclude that if we can better identify and eliminate more distorted dots, this will give us a more accurate wavefront. Going forward, we seek to better refine the accuracy in identifying these distorted dots. Despite our initial success of using values of kurtosis to identify these dots, some distorted dots were still not properly identified. Other mathematical methods such as slope discrepancy and combinations of the central moments, or other image processing methods such as edge detection, maybe beneficial for shock identification.

6. ACKNOWLEDGEMENTS

The authors would like to thank Matt Kalensky for discussions which has been extremely helpful in this work. We also thank Matthew Kemnetz for his comments and insight, especially in regards to the experimental setup. Finally, we would like to thank Zareb Noel and Mark Rennie for helping to develop the digital holography system and related processing codes.

This work was partially funded by the Aerospace and Mechanical Engineering Department at the University of Notre Dame.

REFERENCES

[1] Ben C. Platt, R. S., "History and principles of shack-hartmann wavefront sensing," (2001).

[2] Gordeyev, S. and Jumper, E., "Fluid dynamics and aero-optics of turrets," *Progress in Aerospace Sciences* **46**(8), 388–400 (2010).

[3] Kyrazis, D. T., "Airborne Laser Laboratory departure from Kirtland Air Force Base and a brief history of aero-optics," *Optical Engineering* **52**(7), 1 – 6 (2012).

[4] Jumper, E. J., Zenk, M. A., Gordeyev, S. V., Cavalieri, D. A., and Whitely, M., "Airborne Aero-Optics Laboratory," *Optical Engineering* **52**(7), 1 – 12 (2013).

[5] Bukowski, T. J., Kalensky, M., Gordeyev, S., and Kemnetz, M., "Modal analysis of pressure fields on and around turrets with different protrusions," in [*Unconventional Imaging and Adaptive Optics 2022*], Dolne, J. J. and Spencer, M. F., eds., **12239**, 122390F, International Society for Optics and Photonics, SPIE (2022).

[6] Kalensky, M., Kemnetz, M. R., and Spencer, M. F., "Effects of shock-related discontinuities on SHWFS measurements: modeling and simulation," in [*Unconventional Imaging and Adaptive Optics 2022*], Dolne, J. J. and Spencer, M. F., eds., **12239**, 122390J, International Society for Optics and Photonics, SPIE (2022).

[7] Kalensky, M., Kemnetz, M. R., and Spencer, M. F., "Effects of shock waves on shack–hartmann wavefront sensor data," *AIAA Journal* **61**, 2356–2368 (May 2023).

[8] Southwell, W. H., "Wave-front estimation from wave-front slope measurements," **70**, 998–1006 (1980).

[9] Panda, J. and Adamovsky, G., "Laser light scattering by shock waves," *Physics of Fluids* **7**, 2271–2279 (09 1995).

[10] Kemnetz, M., Kalensky, M., Roeder, A., and Noel, Z., "Effects of shock-related discontinuities on SHWFS measurements: experimental results (Conference Presentation)," in [*Unconventional Imaging and Adaptive Optics 2022*], Dolne, J. J. and Spencer, M. F., eds., **12239**, 122390I, International Society for Optics and Photonics, SPIE (2022).

[11] Kalensky, M., "Branch-point identification using second-moment shack–hartmann wavefront sensor statistics," *Applied Optics* **62**, G101 (May 2023).

[12] Feng, F., Liang, C., Chen, D., Du, K., Yang, R., Lu, C., Chen, S., He, W., Xu, P., Chen, L., Tao, L., and Mao, H., "Moment-based space-variant shack-hartmann wavefront reconstruction," (2023).

[13] Gordeyev, S., Jumper, E., and Whiteley, M., [*Aero-Optical Effects: Physics, Analysis and Mitigation*], Wiley Series in Pure and Applied Optics, Wiley (2023).

[14] Thor Labs, "Shack-hartmann wavefront dwg." [Online; accessed July 28, 2023].

[15] Barchers, J. D., Fried, D. L., and Link, D. J., "Evaluation of the performance of hartmann sensors in strong scintillation," *Appl. Opt.* **41**, 1012–1021 (Feb 2002).

[16] Holmes, R. B., "Scintillation-induced jitter of projected light with centroid trackers," *J. Opt. Soc. Am. A* **26**, 313–316 (Feb 2009).

[17] Nightengale, A. M. and Gordeyev, S., "Shack-hartmann wavefront sensor image analysis: a comparison of centroiding methods and image-processing," *Optical Engineering* **52(7)**, 071413 (2013).

[18] Wilcox, C. C., Radosevich, C. J., Healy, K. P., Tuffli, A. L., Agena, B. D., and Mark F. Spencer, D. J. W. I., "Digital holography wavefront sensing with a super wind tunnel," **11030**, SPIE (2019).

[19] Herráez, M. A., Burton, D. R., Lalor, M. J., and Gdeisat, M. A., "Fast two-dimensional phase-unwrapping algorithm based on sorting by reliability following a noncontinuous path," *Appl. Opt.* **41**, 7437–7444 (Dec 2002).

[20] Gordeyev, S., Burns, R., Jumper, E., Gogineni, S., Paul, M., and Wittich, D., [*Aero-Optical Mitigation of Shocks Around Turrets at Transonic Speeds Using Passive Flow Control*], Grapevine, TX, AIAA Paper 2013-0717 (June 2013).